

Construction of Sensitivity Curves for Dynamic LISA and Taiji

Hong-Yu Shi

*School of Astronomy and Space Science,
University of Chinese Academy of Sciences (UCAS), Beijing 100049, China*

Yong Tang

*School of Astronomy and Space Science,
University of Chinese Academy of Sciences (UCAS), Beijing 100049, China
School of Fundamental Physics and Mathematical Sciences,
Hangzhou Institute for Advanced Study,
UCAS, Hangzhou 310024, China and
International Centre for Theoretical Physics Asia-Pacific, UCAS, Beijing 100190, China*

Abstract

Space-based gravitational-wave (GW) laser interferometers, including LISA and Taiji, are designed to observe gravitational waves in the millihertz band and are expected to open up a frequency range that is otherwise inaccessible. The sensitivity and response of these instruments are central to their scientific goals, mission design and parameter estimation capabilities. However, they are commonly modeled as static, equilateral triangular constellations, an approximation that neglects both orbital motion and directional dependence. In this work, we systematically examine the direction-dependent response and sensitivity of dynamic LISA-like detectors over an entire year of heliocentric orbit. Based on an analytical, time-dependent heliocentric orbital model and an adiabatic unequal-arm interferometer configuration, we construct direction-dependent sensitivity curves in the Michelson interferometric channel for dynamic LISA and Taiji. We obtain analytic expressions for the angular-dependent sensitivity and demonstrate the emergence of a quadrant-like pattern in sky maps at low frequencies. We show that, relative to the static approximation, the low-frequency sensitivity varies by roughly 20%, which in turn produces about a 70% variation in the directional dependence of the number of detectable GW sources, with even larger discrepancies at higher frequencies. Therefore, for accurate predictions of the total GW source counts and reliable parameter inference for binary systems, it is necessary to employ fully dynamic, direction-dependent sensitivity curves.

I. INTRODUCTION

Space-based gravitational-wave (GW) detectors, such as LISA, Taiji and Tianqin [1–3], are designed to detect gravitational waves (GWs) in the millihertz (mHz) frequency band [4, 5]. This frequency band contains a large number of long-lived sources, including massive black-hole binaries, stellar-origin black-hole binaries, extreme mass-ratio inspirals (EMRIs), Galactic compact binaries, and stochastic GW background. Within this frequency range, the orbital motion of the detector makes the instrumental response intrinsically time dependent. For a GW source at a fixed sky position, the detector signal is modulated by the orbital motion, by the changing orientation of the triangular constellation, and by the time evolution of the arm lengths between the spacecraft [4, 5].

The heliocentric constellation, LISA and Taiji, consists of three spacecraft positioned at the vertices of a nearly equilateral triangle, orbiting the Sun in an Earth-trailing configuration. The constellation also performs a cartwheeling motion, so the detector plane and arm directions vary with respect to a fixed source in the sky [4, 5]. The response and sensitivity of LISA-like detectors have been widely analyzed for a static configuration and in an angular-averaged sense [5–18]. These sensitivity curves are typically obtained by combining instrumental noise models with sky and polarization-averaged response functions. Such curves provide convenient references for mission design, population studies, and approximate signal-to-noise-ratio (SNR) estimates. While this static treatment is suitable for characterizing the overall capability of a mission, for a source at a specific sky location the projection between the source direction and the detector arms changes continuously over the observation time. This gives rise to modulation effects both in the response and in the effective sensitivity [19–21]. Consequently, relying solely on the sky-averaged curves may mask direction-dependent variations, and lead to inaccurate estimations for the total number of GW sources and parameter inference of binary systems.

In this work, we systematically investigate the direction-dependent response and sensitivity curves of dynamic LISA-like detectors over a full-year orbiting period. Using a time-dependent heliocentric orbital model and an adiabatic unequal-arm interferometer structure [7, 22], we construct direction-dependent sensitivity curves in Michelson interferometric channel for dynamic LISA and Taiji. At low frequencies, we are able to analytically derive the angular dependent sensitivity curves and show the quadrant pattern in a sky map. We

compare these dynamic sensitivities to the standard static, equal-arm, sky-averaged sensitivities and find that the variation is about 20% in the low-frequency regime, which would lead to 70% variation in the directional dependence of the number of GW sources. And the differences become more pronounced at higher frequencies.

This paper is organized as follows. In Sec. II, we present the theoretical framework, including the signal response of GWs, the Michelson interferometric channel, and the definition of effective strain sensitivity. In Sec. III, we describe the numerical implementation, including the orbital model, time averaging, sky sampling, and the fixed-arm all-sky reference calculation. We illustrate with the dynamic sensitivities in Michelson channel, their comparison with the static equal-arm sky-averaged baseline, the low-frequency directional plateaus, and a full-sky sensitivity map at 3 mHz. We also extend our discussion to other interferometric channels. Finally, in Sec. IV we summarize the main results.

II. THEORETICAL FORMALISM

This section introduces the signal response and sensitivity framework used throughout this work. We first define the GW response of a single inter-spacecraft link and specify the Fourier and delay conventions. We then construct the Michelson channel X , formulate the conventional static equal-arm sensitivity and extend it to a direction-dependent dynamic sensitivity for an evolving unequal-arm constellation.

A. Signal Response and Interferometric Channels

First we introduce the reference frame and conventions in terminology. We denote the unit vector from the Solar System barycenter toward the source as $\hat{\mathbf{N}}$,

$$\hat{\mathbf{N}} = (\sin \theta \cos \phi, \sin \theta \sin \phi, \cos \theta), \quad (1)$$

and by $\hat{\Omega} = -\hat{\mathbf{N}}$ the propagation direction of the GWs, shown in Fig. 1.

In the transverse-traceless gauge, a plane wave propagating along $\hat{\Omega}$ can be written as

$$h_{ab}(t, \mathbf{x}) = \sum_{A=+, \times} h_A \left(t + \frac{\hat{\Omega} \cdot \mathbf{x}}{c} \right) e_{ab}^A(\hat{\Omega}, \psi), \quad (2)$$

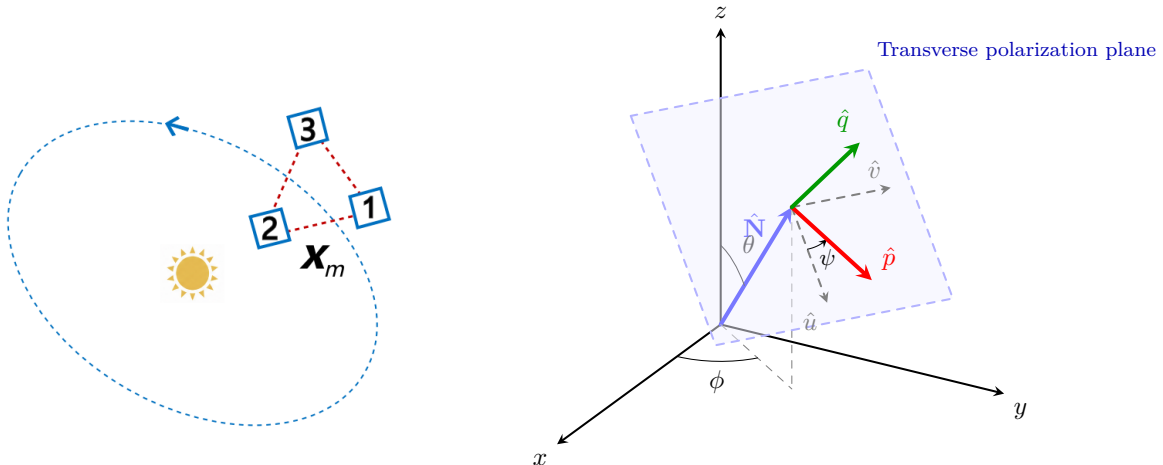


FIG. 1. (left) Schematic illustration of the heliocentric triangular constellation. (right) Coordinate and polarization-basis conventions used in the single-link response calculation. The gravitational-wave propagation direction is $\hat{\Omega} = -\hat{\mathbf{N}}$, where (θ, ϕ) specify the source direction $\hat{\mathbf{N}}$. The vectors \hat{u} and \hat{v} form a sky-fixed transverse basis, while \hat{p} and \hat{q} are obtained by a rotation through the polarization angle ψ .

where $A = +, \times$ labels the two tensor polarizations, $h_A(\tau)$ is the time-domain strain waveform, and $\tilde{h}_A(f)$ denotes its Fourier transform. We use the convention $h_A(\tau) = \int_{-\infty}^{+\infty} \tilde{h}_A(f) e^{-2\pi i f \tau} df$.

$$\hat{u} = (\cos \theta \cos \phi, \cos \theta \sin \phi, -\sin \theta), \quad (3)$$

$$\hat{v} = (-\sin \phi, \cos \phi, 0). \quad (4)$$

These vectors satisfy

$$\hat{u} \cdot \hat{\Omega} = \hat{v} \cdot \hat{\Omega} = 0, \quad \hat{u} \times \hat{v} = \hat{\mathbf{N}} = -\hat{\Omega}. \quad (5)$$

The polarization basis (\hat{p}, \hat{q}) is obtained by rotating (\hat{u}, \hat{v}) through the polarization angle ψ ,

$$\hat{p} = \hat{u} \cos \psi + \hat{v} \sin \psi, \quad (6)$$

$$\hat{q} = -\hat{u} \sin \psi + \hat{v} \cos \psi. \quad (7)$$

The corresponding polarization tensors are

$$e_{ab}^+ = \hat{p}_a \hat{p}_b - \hat{q}_a \hat{q}_b, \quad e_{ab}^\times = \hat{p}_a \hat{q}_b + \hat{q}_a \hat{p}_b. \quad (8)$$

Let $\mathbf{x}_i(t)$ be the barycentric position of spacecraft i . For a laser link between spacecraft i and j , the instantaneous arm length and unit link vector are

$$L_{ij}(t) = |\mathbf{x}_j(t) - \mathbf{x}_i(t)|, \quad \hat{n}_{ij}(t) = \frac{\mathbf{x}_j(t) - \mathbf{x}_i(t)}{L_{ij}(t)}. \quad (9)$$

In this paper, we use the rigid adiabatic approximation, which means we assume the constellation geometry remains static during a single light-travel time, yet we still account for orbital effects on an annual timescale [7].

We adopt the link convention that y_{ij} denotes a measurement of fractional frequency change for the laser light received at spacecraft i from the sending spacecraft j . Following the standard one-way Doppler response [23, 24] and its rigid-adiabatic frequency-domain implementation [25], for a monochromatic plane wave with frequency f , the gravitational-wave contribution to a single-link measurement can be written as

$$y_{ij}(f, t, \hat{\Omega}) = \sum_A \xi_{ij}^A(t, \hat{\Omega}) \left[e^{-2\pi i f \hat{\Omega} \cdot \mathbf{x}_i(t)/c} - e^{+2\pi i f L_{ij}(t)/c} e^{-2\pi i f \hat{\Omega} \cdot \mathbf{x}_j(t)/c} \right] \tilde{h}_A(f) e^{-2\pi i f t}, \quad (10)$$

where the geometric projection factors are

$$\xi_{ij}^+ = -\frac{1}{2} \frac{(\hat{u} \cdot \hat{n}_{ij})^2 - (\hat{v} \cdot \hat{n}_{ij})^2}{1 - \hat{\Omega} \cdot \hat{n}_{ij}}, \quad \xi_{ij}^\times = -\frac{(\hat{u} \cdot \hat{n}_{ij})(\hat{v} \cdot \hat{n}_{ij})}{1 - \hat{\Omega} \cdot \hat{n}_{ij}}. \quad (11)$$

From Eq. (10), it can be seen that, in addition to the phase factor, $e^{-2\pi i f t}$, the time dependence of the single-link response arises from the orbital evolution of the triangular constellation and is encoded in the time-dependent spacecraft positions, instantaneous arm lengths, and link directions.

The above single-link measured quantities are overwhelmed by the laser frequency noise, which motivates the construction of time-delay interferometry channels with virtual equal-arm light paths [6, 22, 26, 27]. For conventional sensitivity curves, one usually considers the Michelson X channel, whose construction is as follows. We define the two round-trip combinations

$$\eta_{12} = y_{12} + \mathcal{D}_{12} y_{21}, \quad \eta_{13} = y_{13} + \mathcal{D}_{13} y_{31}. \quad (12)$$

Here the delay operator is defined as $\mathcal{D}_{ij} y_{mn}(t) = y_{mn}(t - L_{ij}(t)/c)$. The compact unequal-arm Michelson channel is then

$$X(t) = (1 - \mathcal{D}_{13} \mathcal{D}_{31}) \eta_{12} - (1 - \mathcal{D}_{12} \mathcal{D}_{21}) \eta_{13}. \quad (13)$$

Y and Z can be obtained by index cycle ($1 \rightarrow 2 \rightarrow 3 \rightarrow 1$). Here we concentrate on the above first-generation interferometric channels, since our interest lies in their sensitivities, which are identical to those of the corresponding second-generation channels [28].

Note that for fully time-dependent arms, the exact delay operators do not commute. In the frozen-arm adiabatic calculation used here, however, the constellation is held fixed during each instantaneous frequency-domain evaluation, and the delay operators are represented by commuting scalar factors $D_{ij}(f, t) = \exp[+2\pi i f L_{ij}(t)/c]$.

B. Effective strain sensitivity

For an interferometric channel I , the frequency-domain output is written as

$$\tilde{s}_I(f; t) = \tilde{h}_I(f; t, \hat{\Omega}) + \tilde{n}_I(f; t), \quad (14)$$

where \tilde{h}_I and \tilde{n}_I denote the gravitational-wave and instrumental-noise contributions, respectively. The main instrumental noises are the optical metrology system (OMS) noise and the residual acceleration noise of the test masses. Here t labels the slowly evolving orbital configuration of the detector rather than the Fourier-transform variable. At each epoch, the constellation is treated as frozen within the adiabatic approximation. The signal part can be decomposed as

$$\tilde{h}_I(f; t, \hat{\Omega}) = \mathcal{F}_{I,+}(f; t, \hat{\Omega})\tilde{h}_+(f) + \mathcal{F}_{I,\times}(f; t, \hat{\Omega})\tilde{h}_\times(f). \quad (15)$$

where $\mathcal{F}_{I,+}$ and $\mathcal{F}_{I,\times}$ are the complex frequency-domain antenna response functions of channel I to the $+$ and \times polarizations. For a general polarization with angle ψ , we have

$$\mathcal{F}_I(f; t, \hat{\Omega}, \psi) = \mathcal{F}_{I,+}(f; t, \hat{\Omega}) \cos 2\psi + \mathcal{F}_{I,\times}(f; t, \hat{\Omega}) \sin 2\psi. \quad (16)$$

Then averaging over $\psi \in [0, \pi)$ gives the unpolarized response function

$$\mathcal{R}_I(f; t, \hat{\Omega}) \equiv \frac{1}{\pi} \int_0^\pi \left| \mathcal{F}_I(f; t, \hat{\Omega}, \psi) \right|^2 d\psi = \frac{1}{2} (|\mathcal{F}_{I,+}|^2 + |\mathcal{F}_{I,\times}|^2). \quad (17)$$

This quantity is the half trace of the response in the two-dimensional tensor-polarization space and is invariant under a rotation of the polarization basis.

At a fixed orbital time, the effective strain-noise PSD is

$$S_I(f; t, \hat{\Omega}) = \frac{P_I(f; t)}{\mathcal{R}_I(f; t, \hat{\Omega})}, \quad (18)$$

where $P_I(f; t)$ is the instrumental channel-noise PSD, see the appendix for details. In the static equal-arm reference, P_I is time independent. In the dynamic unequal-arm calculation, the underlying noises from optical metrology system and acceleration of test masses are taken to be stationary, while the noise transfer functions may acquire a weak time dependence through the slowly varying arm lengths. The connection between $\tilde{h}_I(f)$ and S_I is that S_I is the effective strain-noise PSD appearing in the SNR integral. Here ρ_I denotes the matched-filtering SNR,

$$\rho_I^2 \simeq 4 \int \frac{|\tilde{h}(f)|^2}{S_I(f; t, \hat{\Omega})} df, \quad (19)$$

up to convention-dependent normalization factors. Because $\rho_I = 1$ is used to set the sensitivity curve, as a function of monochromatic wave $|\tilde{h}_A(f)|$, one may use $\tilde{h}_A(f) \simeq S_I^{1/2}$ for quick estimation.

For the static equal-arm model, we neglect the time dependence of all quantities (except $\exp(-2\pi if t)$) in Eq. 10 and set their values at some reference time $t = t_0$. In such a case the sky-averaged response is defined as

$$\overline{\mathcal{R}}_I^{\text{stat}}(f) = \frac{1}{4\pi} \int \mathcal{R}_I(f; t_0, \hat{\Omega}) d\hat{\Omega}. \quad (20)$$

Its effective strain-noise PSD is

$$S_I^{\text{stat}}(f) = \frac{P_I^{\text{stat}}(f)}{\overline{\mathcal{R}}_I^{\text{stat}}(f)}. \quad (21)$$

For a dynamic constellation orbiting the Sun over the observation time T_{obs} (we shall take it to be one year for sensitivity curves), we define the time-averaged response and channel-noise PSD as

$$\overline{\mathcal{R}}_I^{\text{dyn}}(f; \hat{\Omega}) = \frac{1}{T_{\text{obs}}} \int_0^{T_{\text{obs}}} \mathcal{R}_I(f; t, \hat{\Omega}) dt, \quad \overline{P}_I^{\text{dyn}}(f) = \frac{1}{T_{\text{obs}}} \int_0^{T_{\text{obs}}} P_I(f; t) dt. \quad (22)$$

Here the noise PSD is independent of the source direction, but can acquire a weak time dependence through the slowly varying unequal-arm noise-transfer functions.

Then the annual angle-dependent sensitivity is given by

$$S_I^{\text{dyn}}(f; \hat{\Omega}) = \frac{\overline{P}_I^{\text{dyn}}(f)}{\overline{\mathcal{R}}_I^{\text{dyn}}(f; \hat{\Omega})}. \quad (23)$$

This ratio-of-annual-averages definition preserves the usual noise-to-response form and makes it possible to separate the unequal-arm noise-transfer correction from the directional response correction.

III. NUMERICAL RESULTS

In this section, we shall implement our formalism by numerical simulations. After describing the orbits of three spacecraft and the relevant parameters, we numerically calculate the response function and the sensitivity curves for dynamic Taiji and LISA. In the low-frequency regime, we are able to analytically calculate the sensitivity curves for a general direction. Then we also extend the sensitivity curves for other interferometric channels and discuss the implications of these results.

A. Dynamic sensitivities for Michelson Channel

The spacecraft orbits are modeled using a standard analytic heliocentric triangular configuration with a fiducial arm length L ($L = 2.5 \times 10^9$ m for LISA and $L = 3.0 \times 10^9$ m for Taiji) [4, 5, 7]. The guiding center follows a heliocentric orbit with radius $R = 1$ AU and period $T_{\text{yr}} = 365 \times 24 \times 3600$ s. The orbital eccentricity is chosen as $e = \frac{L}{2\sqrt{3}R}$, so that the mean inter-spacecraft separation is approximately L . The orbital phase is denoted by $\alpha(t) = \frac{2\pi t}{T_{\text{yr}}} + \alpha_0$, where α_0 is the initial orbital phase.

Following the standard analytic heliocentric orbit model expanded to second order in the orbital eccentricity [25], the barycentric positions of spacecraft $m = 1, 2, 3$ are written as $\mathbf{x}_m(t) = (x_m(t), y_m(t), z_m(t))$,

$$x_m = R \cos \alpha + \frac{eR}{2} [\cos(2\alpha - \beta_m) - 3 \cos \beta_m] + \frac{e^2 R}{8} [3 \cos(3\alpha - 2\beta_m) - 10 \cos \alpha - 5 \cos(\alpha - 2\beta_m)], \quad (24)$$

$$y_m = R \sin \alpha + \frac{eR}{2} [\sin(2\alpha - \beta_m) - 3 \sin \beta_m] + \frac{e^2 R}{8} [3 \sin(3\alpha - 2\beta_m) - 10 \sin \alpha + 5 \sin(\alpha - 2\beta_m)], \quad (25)$$

$$z_m = -\sqrt{3} e R \cos(\alpha - \beta_m) + \sqrt{3} e^2 R [\cos^2(\alpha - \beta_m) + 2 \sin^2(\alpha - \beta_m)]. \quad (26)$$

Here the relative phases of the three spacecraft are $\beta_1 = \frac{2\pi}{3}, \beta_2 = \frac{4\pi}{3}, \beta_3 = 2\pi$. The instantaneous arm lengths and link directions are then computed from Eq. (9). In this manner, the slowly changing arm lengths and link orientations are refreshed throughout the yearly orbit. The numerical orbits with precise solar system dynamics would deviate from the above

analytical ones at percent level, which only affect the results at similar level and would not change our main conclusions.

For every direction in the sky, the response is assessed on a daily basis. Within each day, the one-link responses are sampled every $\Delta t = 0.5$ s and averaged to obtain a daily response curve. The dynamic response is then obtained by averaging the daily response curves over the full year.

$$\overline{\mathcal{R}}_I^{\text{dyn}}(f; \hat{\Omega}) = \frac{1}{N} \sum_{i=0}^{N-1} \mathcal{R}_I(f; t_i, \hat{\Omega}), \quad (27)$$

Here N is the total number of samples. This procedure retains the slow orbital breathing of the constellation while using the adiabatic approximation over individual light-travel times.

For comparison, we also compute the static sky-averaged response by numerical integration over a midpoint sky grid

$$\overline{\mathcal{R}}_X^{\text{stat}}(f) \simeq \frac{1}{4\pi} \sum_{a,b} \mathcal{R}_X(f; \theta_a, \phi_b) \sin \theta_a \Delta\theta \Delta\phi. \quad (28)$$

Unless otherwise stated, the grid resolution used for the reference calculation is $N_\theta = 181$ and $N_\phi = 360$.

Figure 2 compares the static reference with the dynamic sensitivities of the 42 directions for one-year observation time, with $\theta \in \{\frac{\pi}{12}, \frac{\pi}{6}, \frac{\pi}{4}, \frac{\pi}{3}, \frac{\pi}{2}, \frac{2\pi}{3}, \frac{5\pi}{6}\}$, $\phi \in \{\frac{\pi}{12}, \frac{\pi}{3}, \frac{2\pi}{3}, \pi, \frac{4\pi}{3}, \frac{5\pi}{3}\}$. In both cases, LISA and Taiji, we notice that the dynamic sensitivity curves (solid lines) scatter around the static one (dashed lines) across the principal millihertz band. And the variation goes to a constant value $\sim 20\%$ at low frequencies but is sizable in the high-frequency regime. Given their similarity, we will concentrate on the Taiji configuration in the remaining discussions.

B. Direction Dependence of the Sensitivity

To quantify the directional difference between the dynamic sensitivity and the static equal-arm sky-averaged reference, we define the ratio

$$\mathcal{Q}_X(f, \hat{\Omega}) = \frac{S_{X,\text{dyn}}^{1/2}(f, \hat{\Omega})}{S_{X,\text{stat}}^{1/2}(f)} \simeq \left[\frac{\overline{\mathcal{R}}_X^{\text{stat}}(f)}{\overline{\mathcal{R}}_X^{\text{dyn}}(f, \hat{\Omega})} \right]^{1/2}. \quad (29)$$

Figure 3 shows \mathcal{Q}_X for a pole direction and for the ecliptic-plane direction $(\theta, \phi) = (\pi/2, \pi/3)$. Both dynamic curves approach nearly frequency-independent plateaus in the

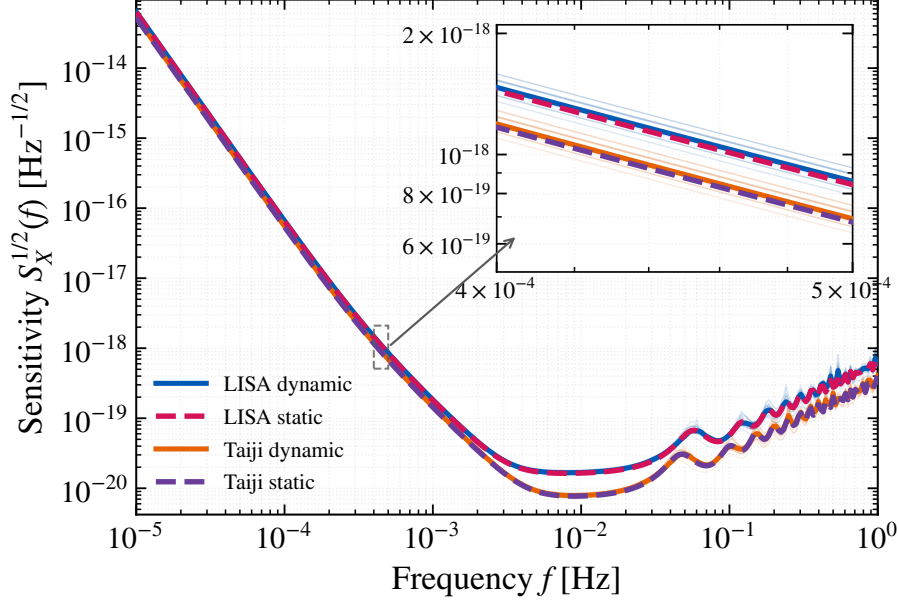


FIG. 2. Direction-dependent sensitivity curves in the X channel for dynamic LISA and Taiji for 42 directions, comparing the dynamic case (solid lines) with the corresponding static sky-averaged references (dashed lines). The inset enlarges the low-frequency region.

long-wavelength/low-frequency regime. The nearly constant plateaus follow from the long-wavelength factorization of the annually averaged dynamic response function,

$$\overline{\mathcal{R}}_X^{\text{dyn}}(f, \hat{\Omega}) \simeq 16 \left(\frac{2\pi f}{c} \right)^4 C_X^{(0)}(\hat{\Omega}), \quad fL/c \ll 1, \quad (30)$$

We calculate the leading angular dependence of the response

$$C_X^{(0)}(\theta, \phi) = \frac{3L^4}{16384} \left[656 + 304 \sin^2 \theta - 74 \sin^4 \theta + 81 \sin^4 \theta \cos \left(4\phi + \frac{\pi}{3} \right) \right], \quad (31)$$

and the corresponding static sky-averaged response,

$$\overline{\mathcal{R}}_X^{\text{stat}}(f) \simeq 16 \left(\frac{2\pi f}{c} \right)^4 C_{X,\text{stat}}^{(0)}, \quad C_{X,\text{stat}}^{(0)} = \frac{3}{20} L^4. \quad (32)$$

The details of the calculations are described in the Appendix B. Note that the common factor f^4 would cancel in the ratio and in the long-wavelength regime we have a frequency-independent

$$\mathcal{Q}_X(f, \hat{\Omega}) \simeq \left[\frac{C_{X,\text{stat}}^{(0)}}{C_X^{(0)}(\hat{\Omega})} \right]^{1/2}. \quad (33)$$

For example, two directions, pole and $(\pi/2, \pi/3)$, give

$$\left[\frac{C_{X,\text{stat}}^{(0)}}{C_X^{(0)}(\text{pole})} \right]^{1/2} = \frac{1}{\sqrt{0.8008}} \simeq 1.1175, \quad \left[\frac{C_{X,\text{stat}}^{(0)}}{C_X^{(0)}(\pi/2, \pi/3)} \right]^{1/2} = \frac{1}{\sqrt{1.131}} \simeq 0.9403, \quad (34)$$

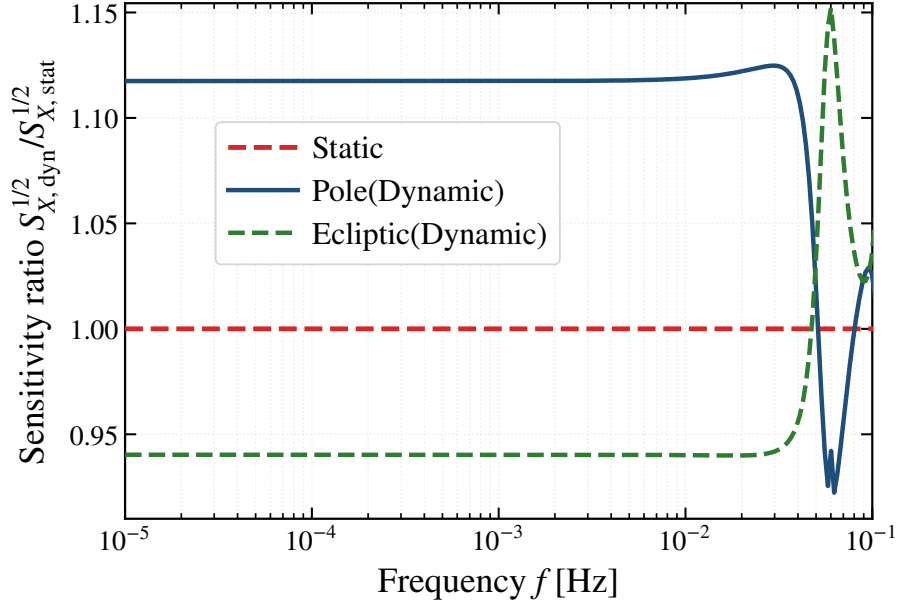


FIG. 3. Ratios relative to the static sky-averaged sensitivity curve. The red line denotes the normalized static reference, the blue curve a pole direction, and the green dashed curve the ecliptic plane direction $(\theta, \phi) = (\pi/2, \pi/3)$. Smaller values mean better sensitivities.

which agree with the numerical evaluation show in Fig. 3 at low frequency $f \lesssim 0.01$ Hz.

In Fig. 4 we plot the dynamic sensitivity over the full sky at $f = 3$ mHz, $S_{X,\text{dyn}}^{1/2}(f = 3 \text{ mHz}, \hat{\Omega})$. Note that lower strain values indicate better sensitivity. We therefore conclude that the triangular constellation is more sensitive to sources located in the directions near the ecliptic plane, while its sensitivity in the polar direction is reduced by about 20%. We also observe the quadrant pattern in the directional dependence, which arises from the last term $\cos(4\phi + \pi/3)$ in Eq. 31, partially reveals the nature of GWs from quadrupole emission.

The above results suggest that the sensitivity would vary about 20% in the low-frequency regime and even more at high frequencies. Because the amplitudes of the GWs are inversely proportional to the distance of the sources r and the volume goes as r^3 in low-redshift universe, the number of detectable GW sources would have a strong directional dependence, up to 70% in the low-frequency regime and much larger at high frequencies. Therefore, for a precise estimation of the number of sources in astronomy and parameter inference, one shall use the dynamic and direction-dependent sensitivity curves. The framework for dynamic sensitivity can also be extended to new physics searches [29–42].

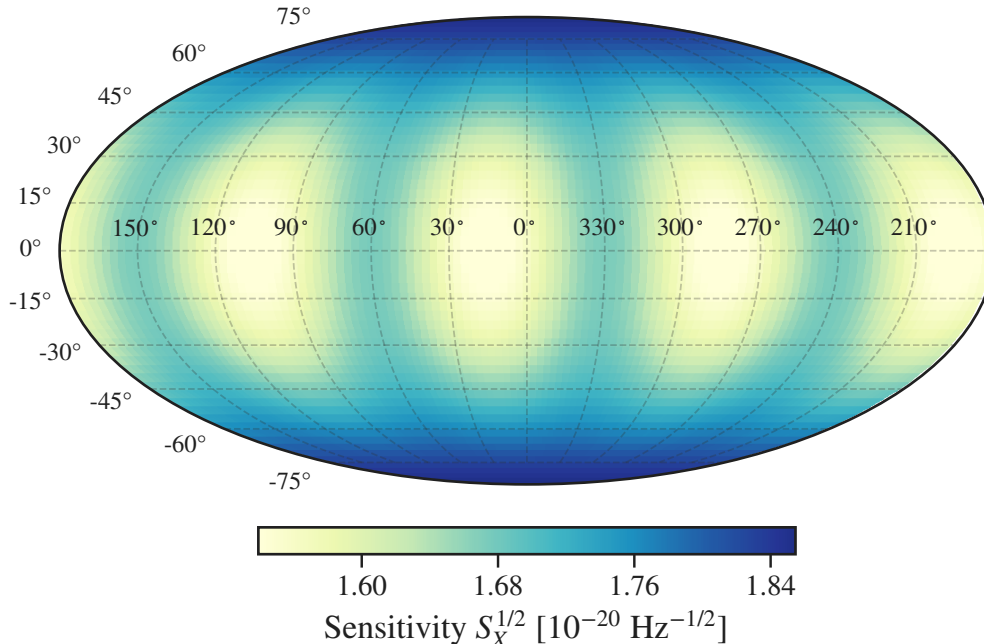


FIG. 4. Directional dependence of sensitivity for dynamic Taiji at $f = 3$ mHz, shown in ecliptic coordinates. Smaller values correspond to better strain sensitivity.

C. Sensitivity Curves for Other Interferometric Channels

In this section, we extend the dynamic sensitivity curves for X to other typical interferometric channels. The three Michelson channels X, Y, Z are commonly recombined into three optimal channels A, E, T [43],

$$A = \frac{1}{\sqrt{2}}(Z - X), \quad E = \frac{1}{\sqrt{6}}(X - 2Y + Z), \quad T = \frac{1}{\sqrt{3}}(X + Y + Z). \quad (35)$$

In the static and equal-arm configuration, the above three channels are orthogonal. A and E have the same sensitivity, and T acts as a nearly null channel. We also consider the first-generation symmetrized-Sagnac variable ζ ,

$$\zeta = \mathcal{D}_{23}(y_{12} - y_{13}) + \mathcal{D}_{31}(y_{23} - y_{21}) + \mathcal{D}_{12}(y_{31} - y_{32}). \quad (36)$$

Fig. 5 shows the static equal-arm sensitivities of $X, A, T,$ and ζ channels, averaging various directions. As shown T and ζ have much worse sensitivity than other two. However, as we shall show in the dynamic case T has the same sensitivity as A and X in the low-frequency regime.

In Fig. 6 we show the dynamic response and sensitivity curves of the X, A, ζ, T channels for the representative direction $(\theta, \phi) = (\pi/4, \pi/3)$. The responses functions of X and A

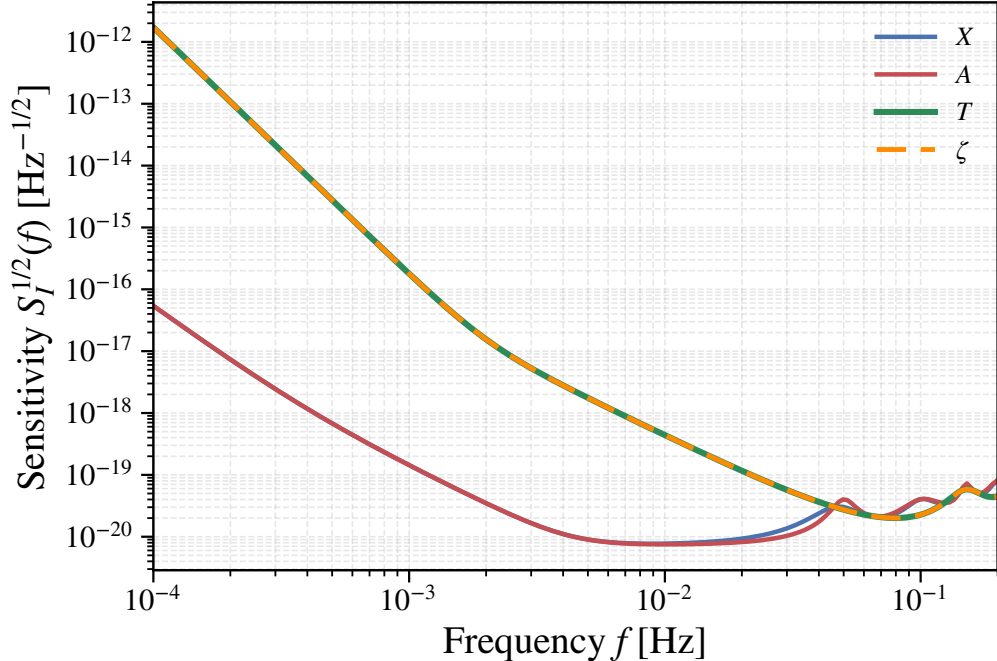


FIG. 5. Static equal-arm sky-averaged amplitude sensitivities of the X, A, T, ζ channels, constructed according to Eq. (21). In the symmetric equal-arm limit, the A and E -channel sensitivities coincide, so only A is shown.

exhibit almost the same low-frequency scaling and their sensitivity curves only differ from their static ones within 20%. However, T and ζ change dramatically in low-frequency regime, see Fig. 7 of comparison to the static case. For the channel T , the reason is that in the dynamic case of the unequal-arms, A, E and T are not orthogonal even more [19, 20]. T gets a modification in the response function and eventually shares the same sensitivity as A and E . For the ζ channel, the modification in the response function is only slightly affected, therefore, its sensitivity is still much worse than the other three, allowing it still as the noise monitor channel [44, 45].

IV. SUMMARY

We have investigated the direction-dependent responses and sensitivity curves of dynamic Taiji and LISA, using an adiabatically evolving unequal-arm triangular constellation with a heliocentric orbit, and compared with the corresponding static equal-arm sky-averaged reference. We have analytically derived the leading angular dependence of the sensitivity

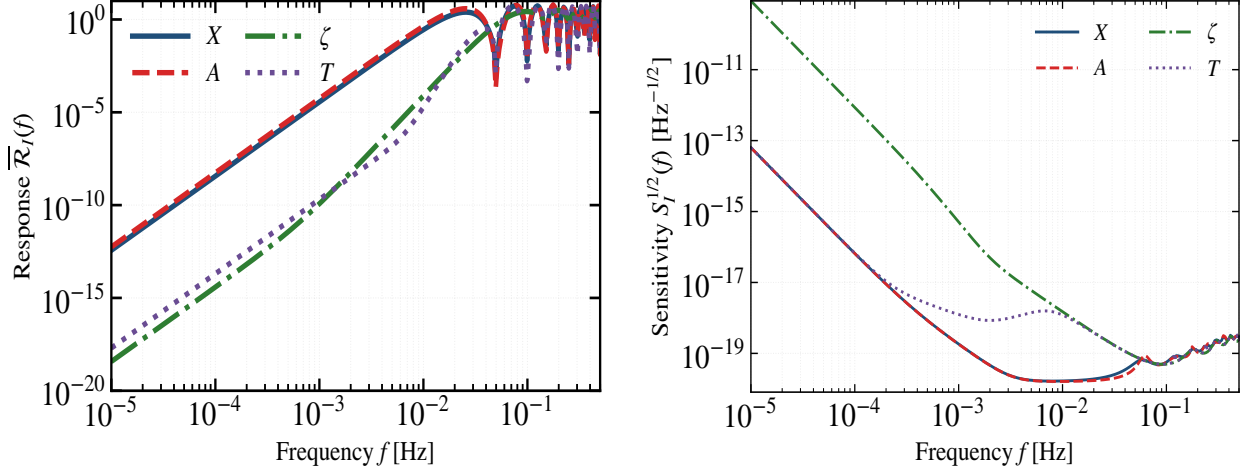


FIG. 6. Dynamic responses and amplitude sensitivities of the X, A, ζ, T channels for $(\theta, \phi) = (\pi/4, \pi/3)$. The left panel shows the response function $\mathcal{R}_I(f)$, and the right panel shows the corresponding sensitivity curves $S_I^{1/2}(f)$.

in the low-frequency/long-wavelength regime ($\lesssim 0.01$ Hz) and found the variation is about 20% in the dynamic case. This would lead to a 70% change in the estimation of the number of GW sources from different directions. At higher frequencies, the variation could be even greater. These results suggest that, for a precise estimation of the number of GW sources and parameter inference of binary systems in astrophysics, one shall use the dynamic and direction-dependent sensitivity curves.

ACKNOWLEDGMENTS

This work is partly supported by the National Key Research and Development Program of China (Grant No. 2021YFC2201901), the National Natural Science Foundation (Grant No.12547104), and the Fundamental Research Funds for the Central Universities.

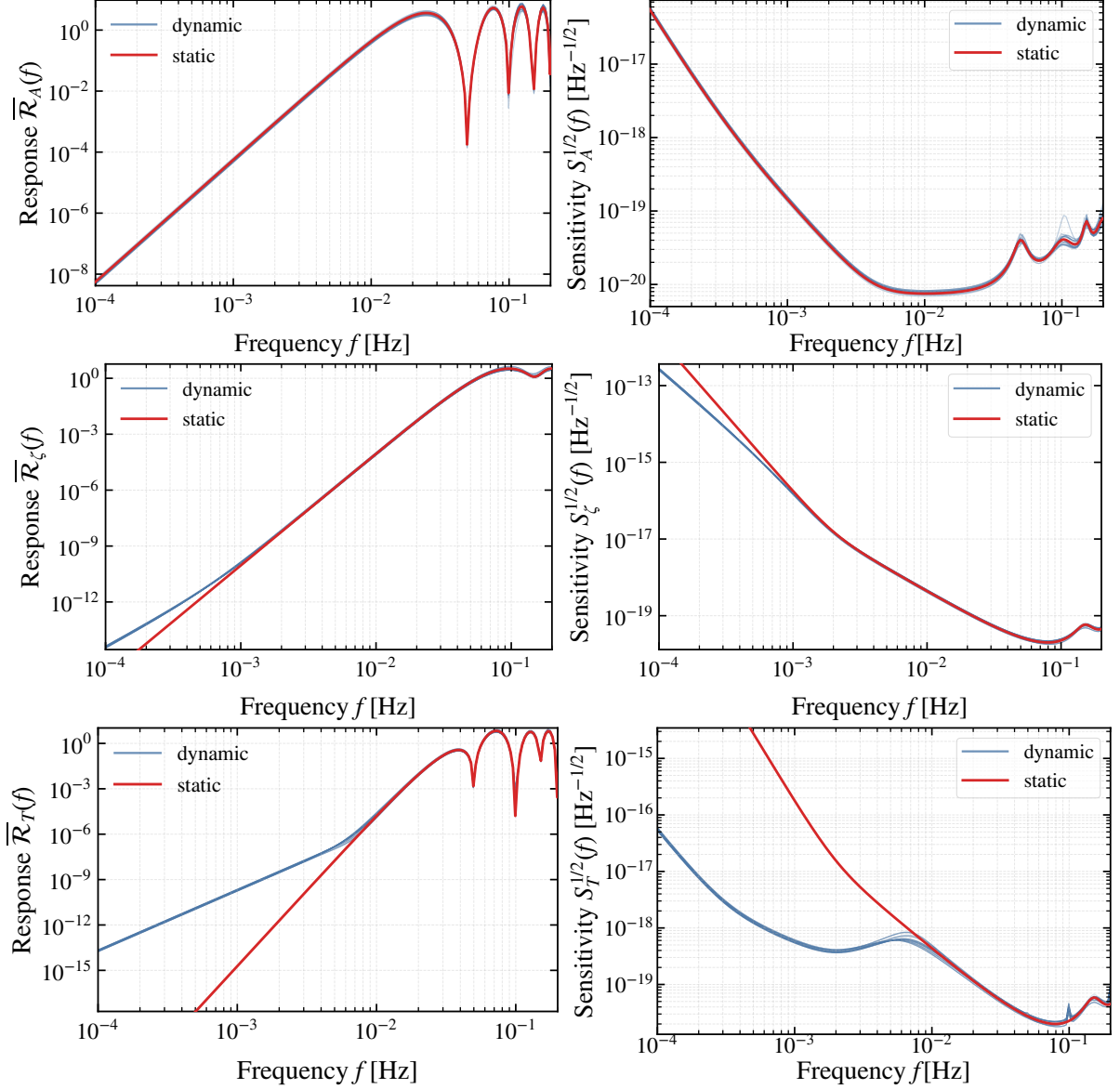


FIG. 7. Dynamic responses and sensitivities for 42 sky directions, compared with the corresponding static equal-arm sky-averaged responses for the A, ζ, T channels, from top to bottom.

Appendix A: Instrumental noises

1. Power Spectral Density (PSD) of noises

The optical metrology noise and test-mass acceleration noise are modeled as [8, 46]

$$S_{\text{oms}}^{1/2}(f) = 15 \times 10^{-12} \frac{2\pi f}{c} \sqrt{1 + \left(\frac{2 \times 10^{-3} \text{ Hz}}{f}\right)^4} \frac{\text{m}}{\sqrt{\text{Hz}}}, \quad (\text{A1})$$

$$S_{\text{acc}}^{1/2}(f) = \frac{3 \times 10^{-15}}{2\pi f c} \sqrt{\left[1 + \left(\frac{0.4 \times 10^{-3} \text{ Hz}}{f}\right)^2\right] \left[1 + \left(\frac{f}{8 \times 10^{-3} \text{ Hz}}\right)^4\right]} \frac{\text{m/s}^2}{\sqrt{\text{Hz}}}. \quad (\text{A2})$$

The numerical coefficient 15×10^{-12} in Eq. (A1) corresponds to the LISA optical metrology noise level. For Taiji, we replace it by 8×10^{-12} , while keeping the same functional form of the OMS noise spectrum.

For the fixed equal-arm compact X variable, the corresponding static noise PSD is

$$P_X^{\text{stat}}(f) = 16 \sin^2\left(\frac{2\pi f L}{c}\right) \left[S_{\text{oms}}(f) + \left(3 + \cos\frac{4\pi f L}{c}\right) S_{\text{acc}}(f) \right]. \quad (\text{A3})$$

Here L is the fiducial arm length of the constellation. This expression is combined with the static sky-averaged response to construct the conventional static equal-arm sensitivity for X -channel. The static noise PSDs of the A , E , and T channels are obtained from the equal-arm X, Y, Z noise covariance, while the static ζ noise PSD is constructed from the same symmetrized-Sagnac combination used for its response.

2. Unequal-arm noise construction

In the dynamic case, the noise spectra in each interferometric channel are constructed directly from the single-link optical metrology and acceleration-noise PSDs in Eqs. (A1) and (A2), using the same adiabatic unequal-arm TDI combinations as those used for the gravitational-wave response.

For each orbital day, we compute the daily mean arm lengths L_{12} , L_{13} , and L_{23} from the time-dependent spacecraft positions. In the present adiabatic approximation, the directed light-travel times are taken to be reciprocal,

$$L_{21} = L_{12}, \quad L_{31} = L_{13}, \quad L_{32} = L_{23}. \quad (\text{A4})$$

The corresponding delay factors are

$$D_{ij}(f) = \exp\left(\frac{2\pi i f L_{ij}}{c}\right). \quad (\text{A5})$$

The positive sign follows from the Fourier convention $e^{-2\pi i f t}$ used in both the response and noise calculations.

For a one-way Doppler link ij , the instrumental-noise contribution is modeled as

$$N_{ij} = n_{ij}^{\text{oms}} + n_{ij}^{\text{acc}} + D_{ij} n_{ji}^{\text{acc}}, \quad (\text{A6})$$

where n_{ij}^{oms} and n_{ij}^{acc} denote independent optical metrology and test-mass acceleration noises associated with the directed link. The round-trip noise combinations are

$$M_{ij} = N_{ij} + D_{ij} N_{ji}. \quad (\text{A7})$$

Explicitly, the noises of the three Michelson variables are

$$X = (1 - D_{13} D_{31}) M_{12} + (D_{12} D_{21} - 1) M_{13}, \quad (\text{A8})$$

$$Y = (1 - D_{21} D_{12}) M_{23} + (D_{23} D_{32} - 1) M_{21}, \quad (\text{A9})$$

$$Z = (1 - D_{32} D_{23}) M_{31} + (D_{31} D_{13} - 1) M_{32}. \quad (\text{A10})$$

This construction retains the frequency-dependent transfer coefficients of each independent underlying OMS and acceleration-noise source.

Equivalently, each Michelson channel can be written as a linear combination of independent noise sources,

$$I(f) = \sum_q C_I^q(f) n_q(f), \quad I \in \{X, Y, Z\}, \quad (\text{A11})$$

where q labels the independent OMS and acceleration-noise components, and $C_I^q(f)$ is the corresponding TDI transfer coefficient.

The noise cross-spectral density matrix is

$$P_{IJ}(f) = \sum_q C_I^q(f) [C_J^q(f)]^* S_q(f), \quad I, J \in \{X, Y, Z\}, \quad (\text{A12})$$

with $S_q = S_{\text{oms}}$ or S_{acc} depending on the type of noise source.

The A , E , and T noise covariance is obtained by applying

$$\begin{pmatrix} A \\ E \\ T \end{pmatrix} = \begin{pmatrix} -1/\sqrt{2} & 0 & 1/\sqrt{2} \\ 1/\sqrt{6} & -2/\sqrt{6} & 1/\sqrt{6} \\ 1/\sqrt{3} & 1/\sqrt{3} & 1/\sqrt{3} \end{pmatrix} \begin{pmatrix} X \\ Y \\ Z \end{pmatrix}. \quad (\text{A13})$$

The diagonal elements of the transformed covariance matrix give $P_A(f)$, $P_E(f)$, and $P_T(f)$, while $P_X(f)$ is obtained from the XX element of Eq. (A12).

For the standard symmetrized-Sagnac channel, the instrumental-noise combination is

$$N_\zeta = D_{23} (N_{12} - N_{13}) + D_{31} (N_{23} - N_{21}) + D_{12} (N_{31} - N_{32}). \quad (\text{A14})$$

Its noise PSD is obtained by expanding Eq. (A14) in the independent OMS and acceleration-noise sources and summing their squared transfer coefficients, in the same manner as Eq. (A12). The response and noise of ζ are therefore evaluated with identical link, delay-phase, and arm-length conventions.

Appendix B: Response function at low frequencies

This section presents the derivation of the nearly constant low-frequency response-ratio plateaus found in Sec. III. The derivation follows the same adiabatic, reciprocal-arm, commuting-delay approximation used in the numerical implementation. It is therefore a low-frequency derivation for the compact TDI model used here, not a second-generation TDI treatment with noncommuting delays [22].

We start from the Michelson channel X ,

$$X = (1 - \mathcal{D}_{13}\mathcal{D}_{31}) \eta_{12} - (1 - \mathcal{D}_{12}\mathcal{D}_{21}) \eta_{13}, \quad (\text{B1})$$

where

$$\eta_{12} = y_{12} + \mathcal{D}_{12}y_{21}, \quad \eta_{13} = y_{13} + \mathcal{D}_{13}y_{31}. \quad (\text{B2})$$

Under the reciprocal-arm approximation,

$$\mathcal{D}_{ij}\mathcal{D}_{ji} \simeq D_{ij}^2, \quad D_{ij} = \exp(+2\pi i f L_{ij}/c). \quad (\text{B3})$$

Define

$$x_{ij}(t) = \frac{2\pi f L_{ij}(t)}{c}. \quad (\text{B4})$$

In the long-wavelength limit $x_{ij} \ll 1$, the one-link gravitational-wave response can be expanded as

$$y_{ij}^A(f, t, \hat{\Omega}) \simeq i x_{ij}(t) d_{ij}^A(t, \hat{\Omega}) h_A(f) + \mathcal{O}(x_{ij}^2), \quad (\text{B5})$$

where

$$d_{ij}^A(t, \hat{\Omega}) = \frac{1}{2} \hat{n}_{ij}^a(t) \hat{n}_{ij}^b(t) e_{ab}^A(\hat{\Omega}) \quad (\text{B6})$$

is the geometrical antenna projection in the low-frequency limit. The apparent denominator in the exact one-link response cancels against the first-order expansion of the propagation phase, leaving the usual quadrupolar projection factor.

Because $D_{ij} = 1 + \mathcal{O}(x_{ij})$ and $d_{ji}^A = d_{ij}^A$, the round-trip combinations become

$$\eta_{12}^A \simeq 2ix_{12}d_{12}^A h_A + \mathcal{O}(x^2), \quad \eta_{13}^A \simeq 2ix_{13}d_{13}^A h_A + \mathcal{O}(x^2). \quad (\text{B7})$$

The delay prefactor similarly gives

$$1 - D_{ij}^2 \simeq -2ix_{ij} + \mathcal{O}(x_{ij}^2). \quad (\text{B8})$$

Substituting Eqs. (B7) and (B8) into Eq. (B1), one obtains the leading-order TDI response

$$X^A(f, t, \hat{\Omega}) \simeq 4 \left(\frac{2\pi f}{c} \right)^2 L_{12}(t) L_{13}(t) \left[d_{12}^A(t, \hat{\Omega}) - d_{13}^A(t, \hat{\Omega}) \right] h_A(f). \quad (\text{B9})$$

Thus the amplitude of X in frequency domain scales as f^2 in the low-frequency limit, and the response function scales as f^4 .

The polarization-averaged response is

$$\mathcal{R}_X(f, t, \hat{\Omega}) = \frac{1}{2} \sum_{A=+, \times} \left| \frac{X^A(f, t, \hat{\Omega})}{h_A(f)} \right|^2. \quad (\text{B10})$$

Using Eq. (B9), we find

$$\mathcal{R}_X(f, t, \hat{\Omega}) \simeq 16 \left(\frac{2\pi f}{c} \right)^4 L_{12}^2(t) L_{13}^2(t) \frac{1}{2} \sum_A \left| d_{12}^A(t, \hat{\Omega}) - d_{13}^A(t, \hat{\Omega}) \right|^2. \quad (\text{B11})$$

Let $\alpha = 2\pi t/T_{\text{yr}}$ be the orbital phase over one year. Then

$$\frac{1}{T_{\text{yr}}} \int_0^{T_{\text{yr}}} dt = \frac{1}{2\pi} \int_0^{2\pi} d\alpha. \quad (\text{B12})$$

The annually averaged response becomes

$$\bar{\mathcal{R}}_X(f, \hat{\Omega}) \simeq 16 \left(\frac{2\pi f}{c} \right)^4 C_X(\hat{\Omega}), \quad (\text{B13})$$

where the direction-dependent geometrical coefficient is

$$C_X(\hat{\Omega}) = \frac{1}{2\pi} \int_0^{2\pi} d\alpha L_{12}^2(\alpha) L_{13}^2(\alpha) \frac{1}{2} \sum_A \left| d_{12}^A(\alpha, \hat{\Omega}) - d_{13}^A(\alpha, \hat{\Omega}) \right|^2. \quad (\text{B14})$$

Eq. (B13) shows that the low-frequency response factorizes into a universal f^4 dependence and a direction-dependent coefficient.

For two directions $\hat{\Omega}_1$ and $\hat{\Omega}_2$, the low-frequency response ratio is therefore

$$\frac{\overline{\mathcal{R}}_X(f, \hat{\Omega}_1)}{\overline{\mathcal{R}}_X(f, \hat{\Omega}_2)} \simeq \frac{C_X(\hat{\Omega}_1)}{C_X(\hat{\Omega}_2)}, \quad fL/c \ll 1. \quad (\text{B15})$$

The same argument applies when one of the two quantities is the sky-averaged response.

The all-sky average is

$$\overline{\mathcal{R}}_X^{\text{stat}}(f) = \frac{1}{4\pi} \int d\hat{\Omega} \overline{\mathcal{R}}_X(f, \hat{\Omega}). \quad (\text{B16})$$

Using Eq. (B13), we obtain

$$\overline{\mathcal{R}}_X^{\text{stat}}(f) \simeq 16 \left(\frac{2\pi f}{c} \right)^4 C_{X,\text{stat}}, \quad (\text{B17})$$

where

$$C_{X,\text{stat}} = \frac{1}{4\pi} \int d\hat{\Omega} C_X(\hat{\Omega}). \quad (\text{B18})$$

Therefore,

$$\frac{\overline{\mathcal{R}}_X(f, \hat{\Omega})}{\overline{\mathcal{R}}_X^{\text{stat}}(f)} \simeq \frac{C_X(\hat{\Omega})}{C_{X,\text{stat}}}, \quad fL/c \ll 1. \quad (\text{B19})$$

For two directions, the same annual-averaged dynamic noise PSD appears in both sensitivities. Their low-frequency ratio is therefore

$$\frac{S_{X,\text{dyn}}^{1/2}(f, \hat{\Omega}_1)}{S_{X,\text{dyn}}^{1/2}(f, \hat{\Omega}_2)} \simeq \sqrt{\frac{C_X(\hat{\Omega}_2)}{C_X(\hat{\Omega}_1)}}. \quad (\text{B20})$$

For the comparison between a dynamic directional sensitivity and the conventional static equal-arm sky-averaged sensitivity, the noise PSDs could be different for other channels I .

The corresponding low-frequency relation is

$$\frac{S_{I,\text{dyn}}^{1/2}(f, \hat{\Omega})}{S_{I,\text{stat}}^{1/2}(f)} \simeq \left[\frac{\overline{P}_I^{\text{dyn}}(f)}{\overline{P}_I^{\text{stat}}(f)} \right]^{1/2} \sqrt{\frac{C_{I,\text{sky}}}{C_I(\hat{\Omega})}}. \quad (\text{B21})$$

The sensitivity ratio therefore contains both the inverse-square-root response factor and a direction-independent noise-transfer factor.

In the leading equal-arm rigid-cartwheel limit, the general low-frequency coefficient $C_X(\hat{\Omega})$ defined in Eq. (B14) reduces to the zeroth-order coefficient $C_X^{(0)}(\hat{\Omega})$. We now derive a closed-form expression for $C_X^{(0)}(\hat{\Omega})$ in this limit. The full numerical calculation used in the main text retains the e^2 orbital terms and the slow arm-length breathing, whereas the expression derived below keeps only the leading equal-arm cartwheeling geometry.

We first introduce the low-frequency detector tensor for the X channel,

$$D_X^{ab}(\alpha) = \hat{n}_{12}^a(\alpha)\hat{n}_{12}^b(\alpha) - \hat{n}_{13}^a(\alpha)\hat{n}_{13}^b(\alpha), \quad (\text{B22})$$

where α is the annual orbital phase. Then

$$d_{12}^A - d_{13}^A = \frac{1}{2}D_X^{ab}e_{ab}^A(\hat{\Omega}). \quad (\text{B23})$$

The polarization sum can be written in terms of the transverse projector

$$P_{ab}(\hat{\Omega}) = \delta_{ab} - \hat{\Omega}_a\hat{\Omega}_b \quad (\text{B24})$$

as

$$\sum_{A=+, \times} e_{ab}^A(\hat{\Omega})e_{cd}^A(\hat{\Omega}) = P_{ac}P_{bd} + P_{ad}P_{bc} - P_{ab}P_{cd}. \quad (\text{B25})$$

Using Eqs. (B23) and (B25), we get the polarization-averaged geometrical factor

$$\mathcal{G}_X(\alpha, \hat{\Omega}) = \frac{1}{2} \sum_A \left| d_{12}^A(\alpha, \hat{\Omega}) - d_{13}^A(\alpha, \hat{\Omega}) \right|^2 = \frac{1}{8} D_X^{ab}(\alpha) D_X^{cd}(\alpha) \Lambda_{abcd}(\hat{\Omega}), \quad (\text{B26})$$

where

$$\Lambda_{abcd}(\hat{\Omega}) = P_{ac}P_{bd} + P_{ad}P_{bc} - P_{ab}P_{cd}. \quad (\text{B27})$$

In the leading-order rigid-cartwheel limit, we use $L_{12} = L_{13} = L$ and obtain the angular factor

$$C_X^{(0)}(\hat{\Omega}) = L^4 \left\langle \mathcal{G}_X^{(0)}(\alpha, \hat{\Omega}) \right\rangle_\alpha, \quad \langle \dots \rangle_\alpha = \frac{1}{2\pi} \int_0^{2\pi} (\dots) d\alpha. \quad (\text{B28})$$

At leading order in the orbital eccentricity, we have the two arm directions

$$\hat{n}_{12}^{(0)} = \left(-\frac{1}{4} \sin 2\alpha, 1 - \frac{1}{2} \sin^2 \alpha, \frac{\sqrt{3}}{2} \sin \alpha \right), \quad (\text{B29})$$

$$\hat{n}_{13}^{(0)} = \left(\frac{1}{4} \cos(2\alpha + \pi/6) - \frac{3\sqrt{3}}{8}, \frac{1}{4} \sin(2\alpha + \pi/6) + \frac{3}{8}, -\frac{\sqrt{3}}{2} \cos(\alpha + \pi/6) \right). \quad (\text{B30})$$

Substituting Eqs. (B29) and (B30) into Eq. (B26) and averaging the resulting trigonometric polynomial over α removes all nonzero orbital harmonics. The remaining closed-form result is

$$C_X^{(0)}(\theta, \phi) = \frac{3L^4}{16384} \left[656 + 304 \sin^2 \theta - 74 \sin^4 \theta + 81 \sin^4 \theta \cos \left(4\phi + \frac{\pi}{3} \right) \right]. \quad (\text{B31})$$

The terms depending only on θ determine the dominant latitude dependence, while the longitude dependence appears as a weaker fourfold modulation.

For a polar source, $\theta = 0$, the longitude is irrelevant and

$$C_X^{(0)}(\text{pole}) = L^4 \frac{123}{1024}. \quad (\text{B32})$$

For a source on the ecliptic plane, $\theta = \pi/2$, Eq. (B31) reduces to

$$C_X^{(0)}\left(\frac{\pi}{2}, \phi\right) = \frac{3L^4}{16384} \left[886 + 81 \cos\left(4\phi + \frac{\pi}{3}\right) \right]. \quad (\text{B33})$$

The sky average of Eq. (B31) is

$$C_{X,\text{stat}}^{(0)} = \frac{1}{4\pi} \int d\hat{\Omega} C_X^{(0)}(\theta, \phi) = \frac{3}{20} L^4, \quad (\text{B34})$$

where we used

$$\langle \sin^2 \theta \rangle_{\text{sky}} = \frac{2}{3}, \quad \langle \sin^4 \theta \rangle_{\text{sky}} = \frac{8}{15}, \quad \langle \cos(4\phi + \pi/3) \rangle_{\phi} = 0. \quad (\text{B35})$$

Therefore, the leading-order response plateau of the polar direction relative to the sky-average is

$$\frac{C_X^{(0)}(\text{pole})}{C_{X,\text{stat}}^{(0)}} = \frac{123/1024}{3/20} \simeq 0.8008. \quad (\text{B36})$$

For the ecliptic-plane direction $\phi = \pi/3$, one obtains

$$\frac{C_X^{(0)}(\pi/2, \pi/3)}{C_{X,\text{stat}}^{(0)}} = \frac{9265}{8192} \simeq 1.131. \quad (\text{B37})$$

-
- [1] P. Amaro-Seoane *et al.*, Laser interferometer space antenna (2017), [arXiv:1702.00786 \[astro-ph.IM\]](#).
 - [2] W.-R. Hu and Y.-L. Wu, [Natl. Sci. Rev.](#) **4**, 685 (2017).
 - [3] J. Luo *et al.*, [Classical and Quantum Gravity](#) **33**, 035010 (2016).
 - [4] C. Cutler, [Phys. Rev. D](#) **57**, 7089 (1998), [arXiv:gr-qc/9703068](#).
 - [5] N. J. Cornish and L. J. Rubbo, [Phys. Rev. D](#) **67**, 022001 (2003), [arXiv:gr-qc/0209011](#).
 - [6] M. Tinto and J. W. Armstrong, [Phys. Rev. D](#) **59**, 102003 (1999).
 - [7] A. Petiteau, G. Auger, H. Halloin, O. Jeannin, E. Plagnol, S. Pireaux, T. Regimbau, and J.-Y. Vinet, [Phys. Rev. D](#) **77**, 023002 (2008), [arXiv:0802.2023 \[gr-qc\]](#).
 - [8] S. L. Larson, W. A. Hiscock, and R. W. Hellings, [Phys. Rev. D](#) **62**, 062001 (2000), [arXiv:gr-qc/9909080](#).

- [9] T. Robson, N. J. Cornish, and C. Liu, *Class. Quant. Grav.* **36**, 105011 (2019), [arXiv:1803.01944 \[astro-ph.HE\]](#).
- [10] T. L. Smith and R. Caldwell, *Phys. Rev. D* **100**, 104055 (2019), [Erratum: *Phys.Rev.D* 105, 029902 (2022)], [arXiv:1908.00546 \[astro-ph.CO\]](#).
- [11] C. Zhang, Q. Gao, Y. Gong, D. Liang, A. J. Weinstein, and C. Zhang, *Phys. Rev. D* **100**, 064033 (2019), [arXiv:1906.10901 \[gr-qc\]](#).
- [12] D. Liang, Y. Gong, A. J. Weinstein, C. Zhang, and C. Zhang, *Phys. Rev. D* **99**, 104027 (2019), [arXiv:1901.09624 \[gr-qc\]](#).
- [13] C. Zhang, Q. Gao, Y. Gong, B. Wang, A. J. Weinstein, and C. Zhang, *Phys. Rev. D* **101**, 124027 (2020), [arXiv:2003.01441 \[gr-qc\]](#).
- [14] X.-Y. Lu, Y.-J. Tan, and C.-G. Shao, *Phys. Rev. D* **100**, 044042 (2019), [arXiv:2007.03400 \[gr-qc\]](#).
- [15] S. Babak, A. Petiteau, and M. Hewitson, arXiv preprint (2021), [arXiv:2108.01167 \[astro-ph.IM\]](#).
- [16] P.-P. Wang, Y.-J. Tan, W.-L. Qian, and C.-G. Shao, *Phys. Rev. D* **103**, 063021 (2021).
- [17] G. Wang, B. Li, P. Xu, and X. Fan, *Phys. Rev. D* **106**, 044054 (2022), [arXiv:2201.10902 \[gr-qc\]](#).
- [18] M. Du, P. Wang, Z. Luo, W.-B. Han, X. Zhang, *et al.*, *Sci. China Phys. Mech. Astron.* **69**, 249501 (2026), [arXiv:2505.16500 \[gr-qc\]](#).
- [19] M. R. Adams and N. J. Cornish, *Phys. Rev. D* **82**, 022002 (2010), [arXiv:1002.1291 \[gr-qc\]](#).
- [20] G. Wang and W.-T. Ni, *Phys. Scripta* **98**, 075005 (2023), [arXiv:2008.05812 \[gr-qc\]](#).
- [21] G. Wang, W.-T. Ni, W.-B. Han, and C.-F. Qiao, *Phys. Rev. D* **103**, 122006 (2021), [arXiv:2010.15544 \[gr-qc\]](#).
- [22] M. Tinto and S. V. Dhurandhar, *Living Rev. Relativity* **8**, 4 (2005), [arXiv:gr-qc/0409034](#).
- [23] F. B. Estabrook and H. D. Wahlquist, *General Relativity and Gravitation* **6**, 439 (1975).
- [24] M. Vallisneri, *Physical Review D* **72**, 042003 (2005), [arXiv:gr-qc/0504145 \[gr-qc\]](#).
- [25] L. J. Rubbo, N. J. Cornish, and O. Poujade, *Physical Review D* **69**, 082003 (2004), [arXiv:gr-qc/0311069 \[gr-qc\]](#).
- [26] M. Tinto, F. B. Estabrook, and J. W. Armstrong, *Phys. Rev. D* **65**, 082003 (2002).
- [27] M. Vallisneri, *Phys. Rev. D* **72**, 042003 (2005), [Erratum: *Phys.Rev.D* 76, 109903 (2007)], [arXiv:gr-qc/0504145](#).

- [28] M. Tinto, S. Dhurandhar, and D. Malakar, *Phys. Rev. D* **107**, 082001 (2023), [arXiv:2212.05967 \[gr-qc\]](#).
- [29] A. Pierce, K. Riles, and Y. Zhao, *Phys. Rev. Lett.* **121**, 061102 (2018), [arXiv:1801.10161 \[hep-ph\]](#).
- [30] S. Morisaki and T. Suyama, *Phys. Rev. D* **100**, 123512 (2019), [arXiv:1811.05003 \[hep-ph\]](#).
- [31] H. Grote and Y. V. Stadnik, *Phys. Rev. Res.* **1**, 033187 (2019), [arXiv:1906.06193 \[astro-ph.IM\]](#).
- [32] A. L. Miller and L. Mendes, *Phys. Rev. D* **107**, 063015 (2023), [arXiv:2301.08736 \[gr-qc\]](#).
- [33] J.-C. Yu, Y.-H. Yao, Y. Tang, and Y.-L. Wu, *Phys. Rev. D* **108**, 083007 (2023), [arXiv:2307.09197 \[gr-qc\]](#).
- [34] Y.-H. Yao and Y. Tang, *Phys. Rev. D* **110**, 095015 (2024), [arXiv:2404.01494 \[hep-ph\]](#).
- [35] Y.-H. Yao, T. Jiang, and Y. Tang, *Phys. Rev. D* **111**, 055031 (2025), [arXiv:2410.22072 \[hep-ph\]](#).
- [36] H.-T. Xu, Y.-H. Yao, Y. Tang, and Y.-L. Wu, *Phys. Rev. D* **112**, 095021 (2025), [arXiv:2506.09744 \[hep-ph\]](#).
- [37] J. Gué, A. Hees, and P. Wolf, *Class. Quant. Grav.* **42**, 055015 (2025), [arXiv:2410.17763 \[hep-ph\]](#).
- [38] Y.-H. Yao, T. Jiang, W. Ren, D. Chen, Y. Tang, and Y.-F. Zhou, (2025), [arXiv:2508.14655 \[hep-ph\]](#).
- [39] R.-M. Yao, X.-J. Bi, P.-F. Yin, and Q.-G. Huang, *JCAP* **04**, 082, [arXiv:2504.10083 \[hep-ph\]](#).
- [40] Y.-Y. Liu, J.-R. Zhang, M.-H. Du, H.-S. Liu, P. Xu, and Y.-L. Zhang, *Eur. Phys. J. C* **86**, 347 (2026), [arXiv:2511.15438 \[gr-qc\]](#).
- [41] J.-R. Zhang, J. Chen, H.-S. Jiao, R.-G. Cai, and Y.-L. Zhang, *Phys. Rev. D* **112**, 064030 (2025), [arXiv:2501.11071 \[gr-qc\]](#).
- [42] Y. Chen, P.-P. Wang, B. Wang, R. Luo, and C.-G. Shao, *Universe* **12**, 48 (2026), [arXiv:2603.07158 \[astro-ph.CO\]](#).
- [43] T. A. Prince, M. Tinto, S. L. Larson, and J. W. Armstrong, *Phys. Rev. D* **66**, 122002 (2002), [arXiv:gr-qc/0209039](#).
- [44] M. Muratore, D. Vetrugno, S. Vitale, and O. Hartwig, *Phys. Rev. D* **105**, 023009 (2022), [arXiv:2108.02738 \[gr-qc\]](#).
- [45] O. Hartwig and M. Muratore, *Phys. Rev. D* **105**, 062006 (2022), [arXiv:2111.00975 \[gr-qc\]](#).
- [46] J.-B. Bayle and O. Hartwig, *Phys. Rev. D* **107**, 083019 (2023).